The Astrophysical Journal Supplement Series, 268:23 (10pp), 2023 September https://doi.org/10.3847/1538-4365/ace7c8

Characterizing the Emission Region Properties of Blazars

Junhui Fan[1,2,3], Hubing Xiao[4], Wenxin Yang[1,2,3], Lixia Zhang[1,2,3], Anton A. Strigachev[5], Rumen S. Bachev[5], and Jianghe Yang[1,6]
[1] Center for Astrophysics, Guangzhou University, Guangzhou, 510006, People's Republic of China; fjh@gzhu.edu.cn
[2] Key Laboratory for Astronomical Observation and Technology of Guangzhou, Guangzhou, 510006, People's Republic of China
[3] Astronomy Science and Technology Research Laboratory of Department of Education of Guangdong Province, Guangzhou, 510006, People's Republic of China
[4] Shanghai Key Lab for Astrophysics, Shanghai Normal University, Shanghai, 200234, People's Republic of China; hubing.xiao@shnu.edu.cn
[5] Institute of Astronomy and National Astronomical Observatory, Bulgarian Academy of Sciences, 72 Tsarigradsko shosse Boulevard, 1784 Sofia, Bulgaria
[6] Department of Physics and Electronics Science, Hunan University of Arts and Science, Changde, 415000, People's Republic of China
Received 2023 April 3; revised 2023 July 12; accepted 2023 July 13; published 2023 September 5

Abstract

Studies and constraints on the emission region are crucial to the blazar radiation mechanism. Yet previous works have mainly focused on individual sources. In this work, we make use of the largest and the latest spectral energy distribution fitting results in the literature to statistically study the blazar emission region properties in the framework of a one-zone leptonic model. Our results reveal: (1) that flat-spectrum radio quasars (FSRQs) show lower electron energy ($\gamma_{\rm p} \lesssim 1.6 \times 10^3$) than BL Lacertae objects (BL Lacs) and tend to have a stronger magnetic field (B) and smaller electron-to-magnetic energy ratio ($U_{\rm e}/U_{\rm B}$) than BL Lacs; (2) we find that the electromagnetic equipartition would rather happen in the jets of BL Lacs than happen in the jets of FSRQs; (3) there are 682 blazars with a magnetic field weaker than the critical value for generating the Kelvin–Helmholtz instability, thus one-third of the blazars in our sample are able to produce this instability; and (4) the distance ($d_{\rm em}$) between the emission region and the central black hole is on the scale of ∼0.1 pc, so the location of the emission region may be evenly distributed inside and outside the broad-line region.

Unified Astronomy Thesaurus concepts: Blazars (164); Flat-spectrum radio quasars (2163); BL Lacertae objects (158); Jets (870); Magnetic fields (994)

Supporting material: machine-readable tables

1. Introduction

Active galactic nuclei (AGNs), one of the most popular extragalactic objects in astronomy, emit radiation in the overall electromagnetic spectrum. The ultimate energy source of AGNs is believed to be the gravitational potential of supermassive black holes (SMBHs), which are embedded in their centers, rather than the nuclear fusion of stars (Lynden-Bell 1969). An accretion disk can be formed surrounding the BHs by matter losing angular momentum before falling onto the BHs (Rees 1984; Cao & Spruit 2013). AGNs are divided into radio-loud and radio-quiet ones, according to their relative radio emission intensity compared to their optical emission intensity (Strittmatter et al. 1980; Kellermann et al. 1989; Xiao et al. 2022c). This dichotomy is mainly caused by the presence of a strong relativistic and collimated jet in the radio-loud AGNs (Urry & Padovani 1995). The jet is so powerful that it dominates the entire emission of radio-loud AGNs, but the mechanism of jet launching is still controversial. Blandford et al. (1977) suggested that the jet is powered by extracting the rotational energy of the BH (the B-Z process), while Blandford & Payne (1982) suggested that the jet is powered by the rotational energy of the accretion disk (the B-P process; see also Xiong & Zhang 2014; Xiao et al. 2022b; Zhang et al. 2022).

Blazars, as an extreme subclass of radio-loud AGNs, exhibit distinctive observational properties. The rapid and large amplitude variability, high and variable polarization, strong and variable γ-ray emissions, and apparent superluminal motion of blazars have been observed and studied (Wills et al. 1992; Urry & Padovani 1995; Fan 2002; Villata et al. 2006; Fan et al. 2014, 2021; Gupta et al. 2016; Xiao et al. 2019, 2020, 2022d; Abdollahi et al. 2020). These properties are believed to be consequences of a Doppler beaming effect, due to a small viewing angle (θ) between the jet axis and line of sight (e.g., Ghisellini et al. 1993; Fan et al. 2013; Pei et al. 2016; Xiao et al. 2020). The Doppler beaming effect is usually pronounced as the time dilation and intensity amplification through a Doppler factor ($\delta = [\Gamma(1 - \beta \cos\theta)]^{-1}$, where Γ is the bulk Lorentz factor and β is the jet speed in units of the speed of light, c), which can be estimated indirectly (Ghisellini et al. 1993; Readhead 1994; Fan 2005; Fan et al. 2013; Liodakis et al. 2018). There are two subclasses of blazars, namely flat-spectrum radio quasars (FSRQs) and BL Lacertae objects (BL Lacs). The former are characterized by an optical spectrum with strong emission lines (rest-frame equivalent width, EW > 5 Å), while the latter demonstrate no or weak emission features (EW < 5 Å; Urry & Padovani 1995; Scarpa & Falomo 1997). Broadband studies illustrate a typical two-hump spectral energy distribution (SED), the lower-energy bump ranging from radio to the X-ray band and peaking at the infrared to X-ray band, which is believed to be the synchrotron emission of the relativistic electrons in the jet, with the higher-energy bump ranging from the X-ray band to the γ-ray band and peaking at the X-ray to GeV γ-ray band (Abdo et al. 2010; Fan et al. 2016; Paliya et al. 2021; Yang et al. 2022, 2023). The radiation mechanism of the higher-energy bump is still controversial; the leptonic model suggests that the higher-energy bump is attributed to the inverse Compton (IC) process (Blandford & Koenigl 1979; Sikora et al. 1994; Sokolov & Marscher 2005; H. E. S. S. Collaboration et al. 2015; Xue et al. 2019; Tan et al. 2020; Wang et al. 2022a), while the hadronic model interprets it through the proton synchrotron radiation and secondary particle cascade (Mücke & Protheroe 2001; Dimitrakoudis et al. 2012; Cerruti et al. 2015; Diltz et al. 2015; IceCube Collaboration et al. 2018; Xue et al. 2021; Wang et al. 2022b).

Broadband SED modeling is an efficient approach to investigate the jet properties, e.g., constraining the magnetic field (B) of the emission region, the Doppler factor, the emission region size (R), and the electron energy distribution (EED; Massaro et al. 2004; Tramacere et al. 2011; Ghisellini et al. 2014; Ghisellini & Tavecchio 2015; Chen 2017). However, there are degeneracies between these critical parameters (Kubo et al. 1998; Ghisellini et al. 2014). Additional methods are employed to further constrain these parameters: for instance, the variability timescale is used to give an upper limit of $R \leqslant c\Delta t\delta/(1+z)$ due to the causality; the Owens Valley Radio Observatory made efforts to estimate δ through the radio lightcurves of blazar flares/outbursts (Liodakis et al. 2018); the Monitoring of Jets in AGN with VLBA Experiments program monitors the radio brightness, polarization variation, and apparent motion (Lister et al. 2015, 2019), with the apparent speed being an indicator of δ (Zhang & Fan 2008; Xiao et al. 2019, 2020); and the polarization observation is critical to the study of blazar magnetic field. The observed polarization shows a frequency dependence of the rotation measure in 3C 273 and suggests that the magnetic field may be structured helically on a large scale (Wardle 2018; Hovatta et al. 2019). Recently, constraining the magnetic field strength with simultaneously observed optical and radio linear polarization and circular polarization was suggested by Liodakis et al. (2022), who proposed a formula of the magnetic field strength being proportional to the square of circular polarization and inversely proportional to the linear polarization. Based on this, they rejected the high-energy emission models requiring high magnetic field strength and a low positron fraction.

It is also possible to determine the magnetic field, Doppler factor, emission region size, etc, via SED features. Kubo et al. (1998) considered a population of relativistic electrons, which forms an EED of a broken power law with a breakpoint at $\gamma_{\rm p}$, and assumed that the lower-energy-component SED peaks at a frequency corresponding to that radiated by the electrons with $\gamma_{\rm p}$. Coupling the assumption with the synchrotron and IC radiation mechanism, they calculated the strength of the magnetic field and the electron Lorentz factor with the energy and intensity of the two SED peaks. Similarly, Chen (2018) applied the same method with a log-parabola EED and obtained formulas to calculate these parameters describing jet properties. Benefiting from the observations of the Fermi Large Area Telescope (LAT), a large number of blazars have been discovered (Abdollahi et al. 2020), and the study of blazars comes to its era of prosperity.

In this work, taking advantage of the latest and largest blazar SED fitting results of Yang et al. (2022) and Yang et al. (2023), we aim to investigate the properties of the blazar emission region and put constraints on those critical parameters. This paper is organized as follows: in Section 2, we present our sample; our method, analysis, and results will be presented in Section 3; the discussions are presented in Section 4; and our conclusions will be given in Section 5.

2. Sample

To study the blazar emission region and constrain its relevant parameters, we need to connect these parameters with observational quantities. We collected a sample of Fermi blazars with the available synchrotron peak frequency ($\log \nu_{\rm sy}$) and corresponding luminosity ($\log L_{\rm sy}$) from Yang et al. (2022) and the IC peak frequency ($\log \nu_{\rm IC}$) and luminosity ($\log L_{\rm IC}$) from Yang et al. (2023). In total, we have 2708 sources, including 759 FSRQs, 1141 BL Lacs, and 808 blazar candidates of uncertain type (BCUs). There are 1791 sources in our sample with available redshift, including 750 FSRQs with an average value of $\langle z_{\rm F}\rangle = 1.201 \pm 0.647$, 843 BL Lacs with average value of $\langle z_{\rm B}\rangle = 0.528 \pm 0.501$, and 198 BCUs with average value of $\langle z_{\rm U}\rangle = 0.919 \pm 0.738$. In this sample, there are 512 blazars associated with sources in Liodakis et al. (2018) and thus with the available Doppler factor (δ), with an average value of $\langle \delta_{\rm F}\rangle = 17.39 \pm 13.42$ for FSRQs, an average value of $\langle \delta_{\rm B}\rangle = 11.26 \pm 10.29$ for BL Lacs, and an average value of $\langle \delta_{\rm U}\rangle = 12.50 \pm 13.37$ for BCUs.

3. Method and Results

3.1. The Basics of the One-zone Leptonic Model

In the leptonic frame, the higher-energy emission results from the IC scattering of internal or external soft photons, namely the synchrotron self-Compton (SSC) and external Compton (EC) processes. The SSC process is believed to dominate the radiation in BL Lacs jets, while the EC process dominates over the SSC process for FSRQs jets. The synchrotron power is mainly produced by those electrons with a Lorentz factor of $\gamma_{\rm p}$ that contribute most to the synchrotron peak, and the synchrotron peak frequency in the observer frame is given by

$$\nu_{\rm sy} = 3.7 \times 10^6\, \gamma_{\rm p}^2\, B\, \frac{\delta}{1+z}\ {\rm Hz}, \tag{1}$$

where B is in units of Gs (Tavecchio et al. 1998). Correspondingly, the synchrotron peak luminosity in the observer frame is expressed as (Chen 2018)

$$L_{\rm sy} = 4\pi\, \frac{16}{9}\pi R^3\, \frac{\sigma_{\rm T} c}{8\pi}\, U_{\rm B}\, N_0\, \gamma_{\rm p}^3\, \delta^4, \tag{2}$$

where $\sigma_{\rm T}$ is the Thomson cross section, $U_{\rm B}$ is the magnetic field energy density ($U_{\rm B} = B^2/8\pi$), and N_0 is the normalization parameter of the EED. Following Chen (2018), a three-parameter log-parabolic function is employed to describe the EED in this work:

$$N(\gamma) = N_0 \left(\frac{\gamma}{\gamma_{\rm p}}\right)^{-3} 10^{-2b\log(\gamma/\gamma_{\rm p})}, \tag{3}$$

where b is the curvature and has a relation with the synchrotron bump, $b \simeq 5P_1$ (see, e.g., Massaro et al. 2006; Chen 2014). This EED is only phenomenologically assumed to follow the log-parabola shape of the SED, without taking into account the evolution due to injection and cooling effects.

Table 1
The Magnetic Field Strength and Electron Energy for 2708 Fermi Blazars

4FGL Name (1)	Class_1 (2)	Class_2 (3)	z (4)	δ (5)	$\log \nu_{sy}$ (6)	$\log \nu_{IC}$ (7)	P1 (8)	$\log B$ (9)	$\log \gamma_p$ (10)	$\log U_e$ (11)	B_c (12)
J0001.2-0747	BLL	ISP			14.1	23.14	−0.12	−2.25	4.46	1.82	28.82
J0001.2+4741	BCU	ISP			14.1	22.50	−0.09	−1.56 ∼ 1.64	4.14 ∼ 2.54	0.68 ∼ −4.26	
J0001.5+2113	FSRQ	LSP	1.11		13.2	20.62	−0.18	2.77	1.47	−5.86	0.004
J0002.4-5156	BCU	HSP			15.7	23.99	−0.09	0.15 ∼ 0.25	4.08 ∼ 4.03	−2.29 ∼ −2.44	
J0003.1-5248	BCU	HSP			15.9	24.31	−0.07	0.23 ∼ 0.13	4.14 ∼ 4.19	−2.24 ∼ −2.09	

Notes. Column (1): the source name. Column (2): the spectral classification. Column (3): the classification based on synchrotron peak frequency (Fan et al. 2016; Yang et al. 2022). Column (4): the redshift. Column (5): the Doppler factor from Liodakis et al. (2018). Columns (6) and (7): the synchrotron and IC peak frequencies from Yang et al. (2022, 2023). Column (8): the spectral curvature from Yang et al. (2022). Column (9): the magnetic field in units of Gs given in this work. Column (10): the energy of the electrons contributing most to the synchrotron peak. Column (11): the energy density of the electrons. Column (12): the critical magnetic field strength. There are only five items displayed here; the table is available in its entirety in machine-readable form.

(This table is available in its entirety in machine-readable form.)

Moreover, if the electrons are in the Thomson regime, the peak frequency of the SSC component is

$$\nu_{\rm SSC} = \frac{4}{3}\,\gamma_{\rm p}^{2}\,\nu_{\rm sy}. \tag{4}$$

In the case of the EC process, where soft photons are fed externally, the peak frequency is given by

$$\nu_{\rm EC} = \frac{4}{3}\,\gamma_{\rm p}^{2}\,\nu_{\rm ext}\,\frac{\Gamma\delta}{1+z}, \tag{5}$$

where $\nu_{\rm ext}$ is the frequency of external photons: $\nu_{\rm ext} = 2.46 \times 10^{15}$ Hz for the case of external photons coming from the broad-line region (BLR) and $\nu_{\rm ext} = 7.7 \times 10^{13}$ Hz for the case of external photons coming from the dusty torus (DT; Tavecchio & Ghisellini 2008; Ghisellini & Tavecchio 2015).

3.2. The Magnetic Field and the Lorentz Factor of Electrons

The magnetic field and the electron energy are crucial to the radiation model of blazar jets. In a leptonic model, one can estimate these two parameters, B and $\gamma_{\rm p}$, through Equations (1), (4), and (5) in both the SSC and EC processes. We calculated B and $\gamma_{\rm p}$ for the 1900 blazars, including 1141 BL Lacs and 759 FSRQs, where the SSC process is assumed to be the emission case of the BL Lacs and the EC process is considered for the FSRQs. An average replacement is used for those sources without available redshift or Doppler factors: $\langle z_{\rm F}\rangle = 1.21$ and $\langle \delta_{\rm F}\rangle = 17.47$ for FSRQs and $\langle z_{\rm B}\rangle = 0.528$ and $\langle \delta_{\rm B}\rangle = 11.26$ for BL Lacs. In addition, for the EC process in FSRQs, we consider the external photons from the DT for those high-synchrotron-peaked blazars (HSPs) and the external photons originating from the BLR for those low-synchrotron-peaked blazars (LSPs) and intermediate-synchrotron-peaked blazars (ISPs). In this case, we have 754 FSRQs using the model of external soft photons coming from the BLR; this is consistent with the assumption of a soft photon origin for FSRQs in the literature (e.g., Tan et al. 2020) and also consistent with the facts that the FSRQs show significant broad emission lines and the emission lines contribute to the EC component significantly (Xiao et al. 2022a). The rest of the five FSRQs are considered as HSPs, and the HSPs are naturally considered as TeV candidates (Zhu et al. 2023). The TeV emission could be severely absorbed by interacting with BLR soft photons, thus we assume these five FSRQs with soft photons are from the DT. The results of $\log B$ and $\log \gamma_{\rm p}$ are listed in columns (9) and (10) of Table 1 and are displayed in Figure 1. A Gaussian fit is applied to the distributions, and the fitting results give a mean value of $\log B^{\rm B} = -0.51$ with a standard deviation of 1.66 for the BL Lacs and a mean value of $\log B^{\rm F} = 1.76$ with a standard deviation of 0.85 for the FSRQs, as well as a mean value of $\log \gamma_{\rm p}^{\rm B} = 4.17$ with a standard deviation of 0.32 for BL Lacs and a mean value of $\log \gamma_{\rm p}^{\rm F} = 2.01$ with a standard deviation of 0.43 for FSRQs. A two-sample Kolmogorov–Smirnov (K-S) test is employed to test whether each parameter for these two subclasses is from the same parent distribution. In the K-S test, a probability smaller than the critical value ($p = 0.05$) would be used to reject the null hypothesis, which is that the two distributions are coming from the same parent distribution. Our results of the K-S tests show $p \sim 0$ for both the $\log B$ and $\log \gamma_{\rm p}$ distributions, suggesting the BL Lac $\log B^{\rm B}$ distribution and the FSRQ $\log B^{\rm F}$ distribution come from different parent distributions, as do the BL Lac $\log \gamma_{\rm p}^{\rm B}$ distribution and the FSRQ $\log \gamma_{\rm p}^{\rm F}$ distribution.

Besides, we calculate the range of both $\log B$ and $\log \gamma_{\rm p}$ for the 808 BCUs in our sample; the limits are obtained by assuming the seed photons come from either the SSC or from the EC. During the calculation, the average replacement is used for those BCUs without available redshift and Doppler factors. The results are listed in columns (9) and (10) of Table 1.

3.3. The Emission Region of Blazars

The jet emission region size (R) is usually constrained by a causality reason, which is the variability timescale, and expressed as

$$R \leqslant c\,\Delta t\,\frac{\delta}{1+z}. \tag{6}$$

R is easily obtained if we assume a variability timescale Δt for those blazars with available z and δ. Throughout this paper, we assume $\Delta t = 1$ day (Fan et al. 2013; Nalewajko 2013) to estimate R. Consider a constant and symmetric jet geometry. If the full jet cross section is responsible for the emission region diameter, then the distance from the central SMBH to the emission region $d_{\rm em}$ and the emission region size R are

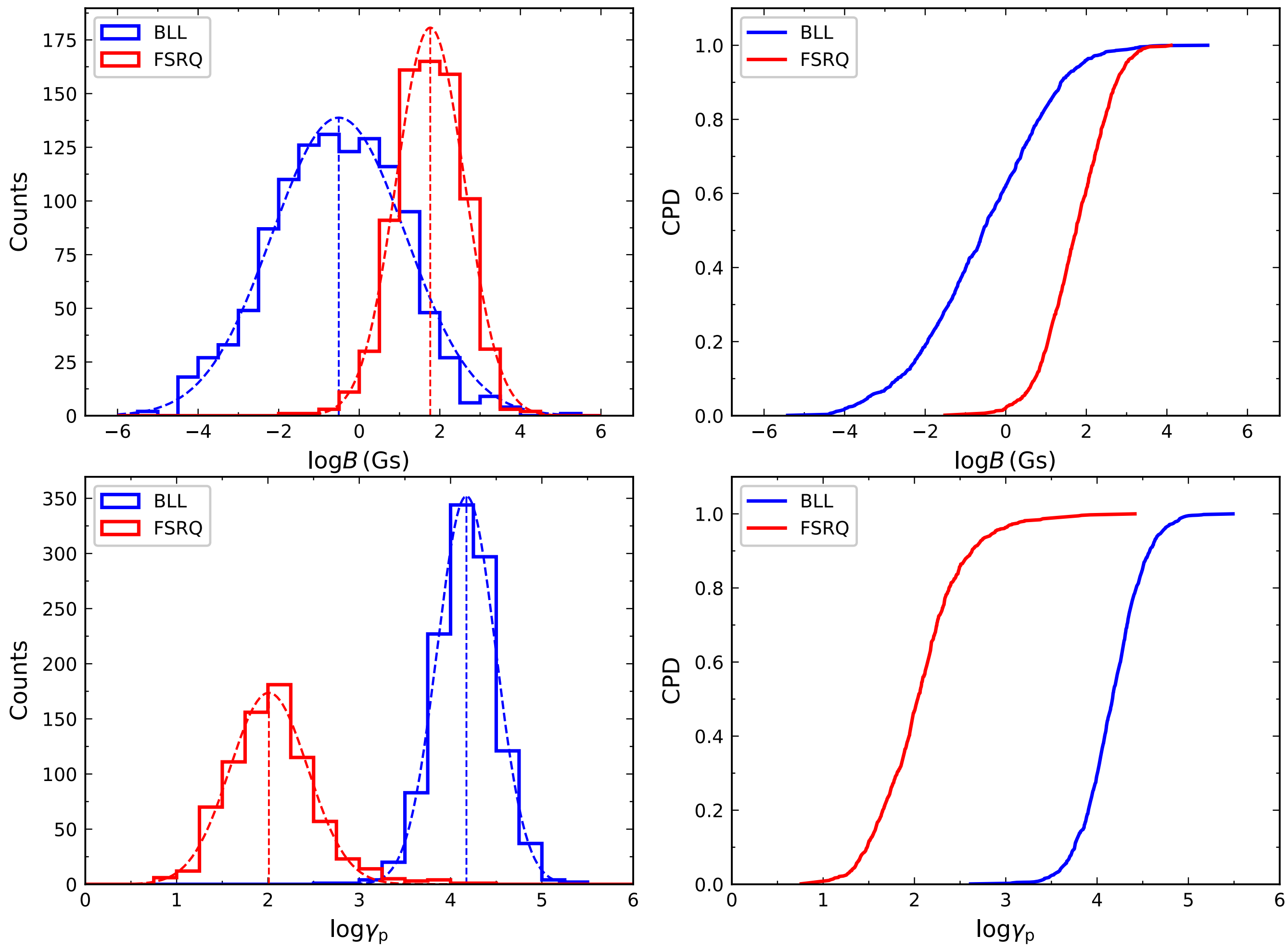

Figure 1. The distributions of B and γ_p. The left panels give the distributions of the two parameters, with the dashed curve standing for the Gaussian fit of the histogram. The right panels give the corresponding cumulative probability distributions. The red color stands for FSRQs and the blue color stands for BL Lacs throughout this paper.

correlated as

$$R = d_{\rm em} \tan\phi, \tag{7}$$

where ϕ is the semi-aperture opening angle of the jet (Acharyya et al. 2021). ϕ is an undetectable quantity, the value of $\tan\phi = 0.1$ is fixed to the study of blazar jet power in Ghisellini & Tavecchio (2009), and $\tan\phi \lesssim 0.25$ is suggested in Dermer et al. (2009). In this work, we can assume this opening angle ϕ to be close to the viewing angle θ for blazars ($\theta \simeq \phi$), due to the fact that the blazar jet is pointing at observers. Actually, θ can be estimated by using the apparent velocity of the resolved jet components and is expressed as

$$\tan\phi \simeq \tan\theta = \frac{2\beta_{\rm app}}{\beta_{\rm app}^2 + \delta^2 - 1}, \tag{8}$$

where $\beta_{\rm app}$ is the apparent velocity of the jet component (Kellermann et al. 2004; Liodakis et al. 2018; Xiao et al. 2019), which is usually observed via the Very Long Baseline Interferometry technique (Lister et al. 2009, 2019, 2021). We manage to collect θ from Liodakis et al. (2018) for 182 blazars (35 BL Lacs and 147 FSRQs) of our sample and list them in column (5) of Table 2, showing them in Figure 2. We notice that 142 of 147 FSRQs have $\tan\theta < 0.25$, which is 96.9%, and 30 of 35 BL Lacs have $\tan\theta < 0.25$, which is 85.7%. Then we calculate the $d_{\rm em}$ for these 182 sources and list the results in column (6) of Table 2, showing them in Figure 3. The distribution of the emission region distance gives a mean value $\log d_{\rm em}^{\rm B} = 17.37$ with a standard deviation of 0.91 for BL Lacs and $\log d_{\rm em}^{\rm F} = 17.49$ with a standard deviation of 0.88 for FSRQs. A K-S test result of 0.31 suggests that the $\log d_{\rm em}^{\rm B}$ and $\log d_{\rm em}^{\rm F}$ could come from the same distribution.

4. Discussions

4.1. The Energy Density of the Relativistic Electron Population

In the system of a BH-based jet, the particle field relations depend on uncertain jet formation, particle acceleration, and radiation mechanisms (Dermer et al. 2014). It is natural that systems with interacting components often tend to equipartition. As a synchrotron source, a blazar jet contains relativistic electrons with some energy density $U_{\rm e}$ and a magnetic field whose energy density is $U_{\rm B} = B^2/(8\pi)$. In order to avoid involving those poorly understood microphysics processes in the jets, Dermer et al. (2014) assumed a condition that the equipartition between the magnetic field and nonthermal electron energy densities holds for blazar jets, as was used in the analysis of a wide variety of astrophysical systems; see Burbidge (1959) for the radio lobes,

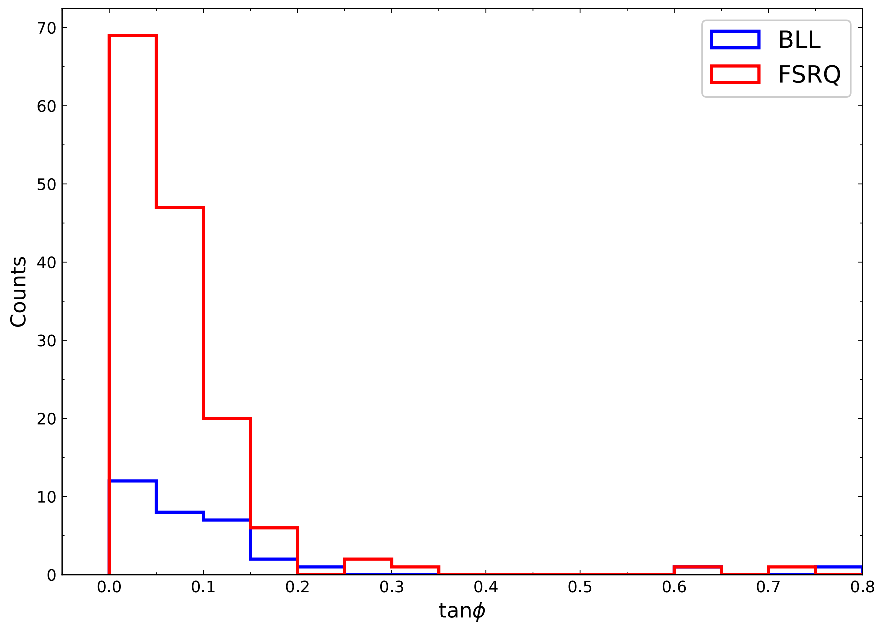

Figure 2. The distribution of $\tan \phi$.

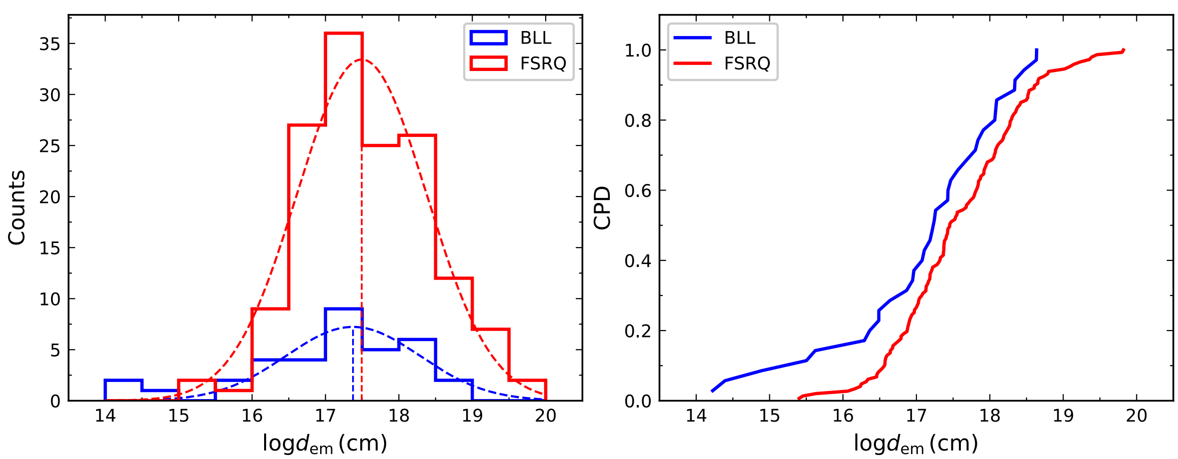

Figure 3. The distribution of $\log d_{\rm em}$.

Table 2
The Location of the Emission Region for 182 Blazars

4FGL Name (1)	Class_1 (2)	z (3)	δ (4)	θ (5)	$\log d_{\rm em}$ (6)	$\log d_{\rm em}$ (G15) (7)	$\log L_{\rm BLR}$ (8)
J0006.3-0620	BLL	0.346676	6.96	8.25	16.97		43.60
J0017.5-0514	FSRQ	0.227	12.02	0.72	18.31	16.17	43.77
J0019.6+7327	FSRQ	1.781	7.84	7.32	16.75		45.62
J0051.1-0648	FSRQ	1.975	5.61	7.27	16.58		46.11
J0102.8+5824	FSRQ	0.644	18.51	2.39	17.84	16.75	45.04

Note. Column (1): the source name. Column (2): the spectral classification. Column (3): the redshift. Columns (4) and (5): the Doppler factor and the viewing angle from Liodakis et al. (2018). Column (6): the estimated $\log d_{\rm em}$ from this work. Column (7): the estimated $\log d_{\rm em}$ in Ghisellini & Tavecchio (2015). Column (8): the luminosity of the BLR from Xiao et al. (2022b). There are only five items displayed here; the table is available in its entirety in machine-readable form.

(This table is available in its entirety in machine-readable form.)

Pacholczyk (1970) for a study of radio sources, and Beck & Krause (2005) for a theoretical equipartition study of synchrotron observations. On large scales, the equipartition also corresponds to the minimum jet power condition as suggested by Ghisellini & Celotti (2001), in which the minimum jet power is required to produce the radiation we observe at all wavelengths. The simplest equipartition relation is $U_{\rm e} = \xi U_{\rm B}$, where ξ is close to unity (Ghisellini & Celotti 2001; Dermer et al. 2014). It is believed that the jet is in global equipartition between U_e and U_B; however, local instances where it is out of equipartition are also allowed to explain peculiar observation phenomena. The very-high-energy detection of 3C 279 (MAGIC Collaboration et al. 2008) required either emission from leptons far out of equilibrium accompanied by poor fits to the X-ray or synchrotron data in the leptonic frame. In 2018, Fermi observed a characteristic peak-in-peak variability pattern on timescales in minutes of 3C 279 resulting from magnetic reconnection (Shukla & Mannheim 2020).

In Figure 1, we notice that the FSRQs show a stronger magnetic field than the BL Lacs, while the latter show a higher energy of electrons than the former. This is consistent with the typical blazar radiation mechanism paradigm, in which FSRQs contain a photon-rich environment, so that the energy of relativistic electrons in the emission blob could efficiently dissipate via the IC process. And BL Lacs are believed to be located in a photon-starving environment, thus the accelerated relativistic electrons can be well preserved. Moreover, the distribution of $\log \gamma_p$ shows a clear separation between the FSRQs and the BL Lacs. This result reveals the energy of the relativistic electrons is distributed over a wide range, which contains large variance for different types of blazars, the FSRQs taking the side of lower energy, with the BL Lacs taking the side of higher energy. We suggest using the intersection point value, $\log \gamma_p = 3.20 \pm 0.01$ ($\gamma_p \simeq 1.6 \times 10^3$), of the two Gaussian profiles to divide the FSRQs and BL Lacs.

With known B, γ_p, and $N(\gamma)$, one can obtain the magnetic energy density U_B and the electron energy density

$$U_e = \int_{\gamma_{min}}^{\gamma_{max}} \gamma \, m_e c^2 N(\gamma) d\gamma, \quad (9)$$

where the minimum Lorentz factor $\gamma_{min} = 10$ and maximum Lorentz factor $\gamma_{max} = 1 \times 10^6$ of the electrons are assumed, and m_e is the rest mass of electron. Figure 4 shows the distribution of $\log U_e$ and the ratio $\log(U_e/U_B)$. The Gaussian fit gives results of a mean value $\log U_e^B = -1.47$ with a standard deviation of 3.12 for BL Lacs and $\log U_e^F = -4.40$ with a standard deviation of -2.14 for FSRQs, as well as a mean value $\log(U_e^B/U_B^B) = 0.98$ with a standard deviation of 6.23 for BL Lacs and a mean value $\log(U_e^F/U_B^F) = -6.45$ with a standard deviation of 3.68 for FSRQs. The K-S tests of $\log U_e$ and $\log(U_e/U_B)$ for BL Lacs and FSRQs both give results of $p \sim 0$. The results suggest $\log U_e^B$ and $\log U_e^F$ are from different distributions, as are $\log(U_e^B/U_B^B)$ and $\log(U_e^B/U_B^F)$. Based on our results shown in Figures 1 and 4, we suggest BL Lacs have an averagely larger energy and energy density of electron distribution, while they also show a larger electron-to-magnetic energy ratio than FSRQs.

Based on the distribution of $\log(U_e/U_B)$ in Figure 4, it is clear that most of the FSRQs are away from the value $\log(U_e/U_B) = 0$, which is the condition of equipartition between magnetic field and nonthermal electron energy densities, while the BL Lacs have a mean value near $\log(U_e/U_B) = 0$. Thus, our results suggest that the BL Lacs stay in a "quasi-equipartition" state, while the FSRQs do not.

4.2. The Kelvin–Helmholtz Instability

Variation, one of the characterizing properties of blazars, has been observed across all frequencies and timescales (e.g., Urry 1996; Dermer 1999; Fan 1999; Singh & Meintjes 2020; Webb et al. 2021; Amaya-Almazán et al. 2022; Otero-Santos et al. 2022). Blazar variability timescales are observed from years to months, to days, and even to minutes (Wagner & Witzel 1995; Fan et al. 1998, 2018; Aharonian et al. 2007; Albert et al. 2007). The basic idea of the mechanism for these different timescales of variabilities is that a disturbance created near the BH travels outward with a Lorentz factor Γ and radiates energy at a distance $\gtrsim \Gamma^2 r_g$, where r_g is the gravitational radius. This scenario works for most of the cases of variability in the optical, X-ray, and even γ-ray bands; together with those models referring to the jet spiral structure, precession, or geometric effects in the jet (Camenzind & Krockenberger 1992; Gopal-Krishna & Wiita 1992), all the blazar variability seems mostly well explained. Minute timescale variability observed in the TeV band (Aharonian et al. 2007; Albert et al. 2007) demands every efficient particle acceleration/dissipation mechanism (Shukla & Mannheim 2020; Wang et al. 2022a) or an extremely small emission zone. Although the variability mechanisms have been explored and discussed by many people, the initial seed instability of the arising blazar variabilities, over different timescales, has been little discussed.

A two-fluid model, which was proposed by Sol et al. (1989), coupled with the Kelvin–Helmholtz instability could have a chance. In this scenario, two fluids (one fluid is a nonrelativistic jet with electron–proton plasma, and the other one is a relativistic jet with an electron–positron plasma) with different speeds and compositions, the Kelvin–Helmholtz instability occurs at the junction of the two jet components and generates significant disturbances (Romero 1995; Cai et al. 2022). But this instability only happens when the magnetic field is weaker than the critical magnetic field strength

$$B_c = [4\pi N m_e c^2 (\Gamma^2 - 1)]^{1/2} \Gamma^{-1}, \quad (10)$$

where N is the particle number density that we obtained via Equation (3) and Γ is assumed to be equal to δ. We calculate the B_c for the FSRQs and BL Lacs in our sample, and an average value replacement is applied to those sources without available δ during the calculation; the results are listed in column (12) of Table 1. Based on our calculation, there are 682 sources (36% of the sources of the FSRQs and BL Lacs) that have a magnetic field weaker than the critical one. The result suggests that there are a significant number of Fermi blazars that could show the Kelvin–Helmholtz instability in the emission zone. There are possible consequences of these instabilities. The instability could be amplified due to accumulation, thus showing detectable variability, and the variability timescale is dependent on the energy dissipation efficiency. Or the instability could be generated in the manner of a kink and thus show detectable violent variability. For instance, these kink instabilities can disrupt the jet (Porth & Komissarov 2015; Barniol Duran et al. 2017) and trigger magnetic reconnection (Giannios & Spruit 2006; Shukla & Mannheim 2020). The magnetic reconnection accelerates particles, and these particles dissipate rapidly over a very short timescale, e.g., the 3C 279 γ-ray flare (Shukla & Mannheim 2020).

With the assumption of the two-fluid model Kelvin–Helmholtz instability, our results suggest that more than one-third of the blazars are able to show this instability. Although the result is still modest if we consider that the observed

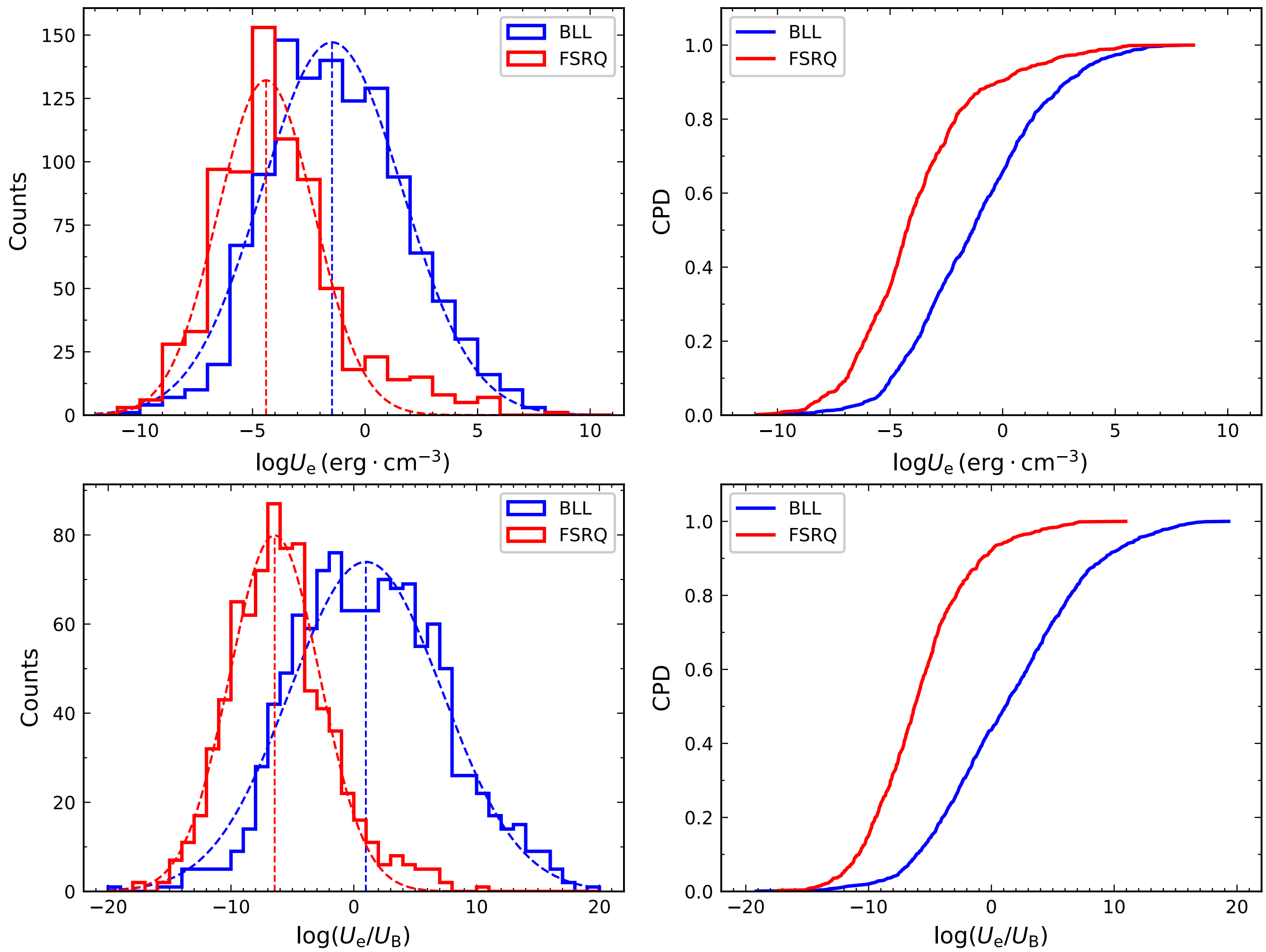

Figure 4. The distributions of $\log U_{\rm e}$ and $\log(U_{\rm e}/U_{\rm B})$.

variabilities are initially arising from the seed instabilities because almost all the observed blazars show strong variabilities, although these variabilities happen in different bands and at different epochs. The possible reasons are the following: (1) the SED fitting results of the particle number density, which we applied to calculate $B_{\rm c}$, are biased by high states of blazars; or (2) other mechanisms of seed instability, which were not considered in this work, may be involved. However, one should keep in mind that even if all the blazars can generate instabilities, the strong and violent variability only happens occasionally, because most of the instabilities fade before they are amplified to generate significant variabilities.

4.3. The Location of the Emission Region

The location of the emission region is one of the essential properties in blazars. In the framework of the one-zone leptonic model, emissions in different bands are believed to be radiated in the same region. However, the location of the blazar emission region is controversial. The most common method to determine the location of the emission region is by assuming a constant jet geometry and taking the full jet cross section as the emission region diameter, then obtaining the distance between the emission region and the SMBH through the basic trigonometric relations. Foschini et al. (2011) used ∼2 yr of Fermi-LAT observations to study the locations of several blazars and found the location should be within the BLR. The expected spectral cutoff, arising from the photon–photon pair annihilation of γ-rays with a helium Lyman recombination continuum within the BLR (Poutanen & Stern 2010), at the GeV band is not always observed. Not even the cutoff could be explained by another consequence, e.g., a break on the EED, as suggested by Dermer et al. (2015). Furthermore, the detection of TeV emission from blazars suggests the TeV emission region should locate outside the BLR; because of the severe attenuation, the interactions between TeV photons and the photons in the BLR would not allow us to observe the TeV emission from blazars.

In this work, we have focused our research on the location of the blazar emission region. We applied a timescale of 1 day, which was suggested by Nalewajko (2013); as a typical variability timescale in the source frame in the Fermi γ-ray band, this timescale has been used in many works (e.g., Ghisellini et al. 1998; Fan et al. 2013; Nalewajko 2013; Chen 2018; Pei et al. 2022). One can set an upper limit on the emission region size via inequality (6), thus its distance from the SMBH can be estimated via Equation (7). An approximation, which assumes the viewing angle to be equal to the jet semi-opening angle, is proposed and employed in this work. We notice that most of our sources have semi-opening angles of $\tan\phi < 0.25$; see the upper panel of Figure 3. Our result is partly consistent with the range for the semi-opening angle,

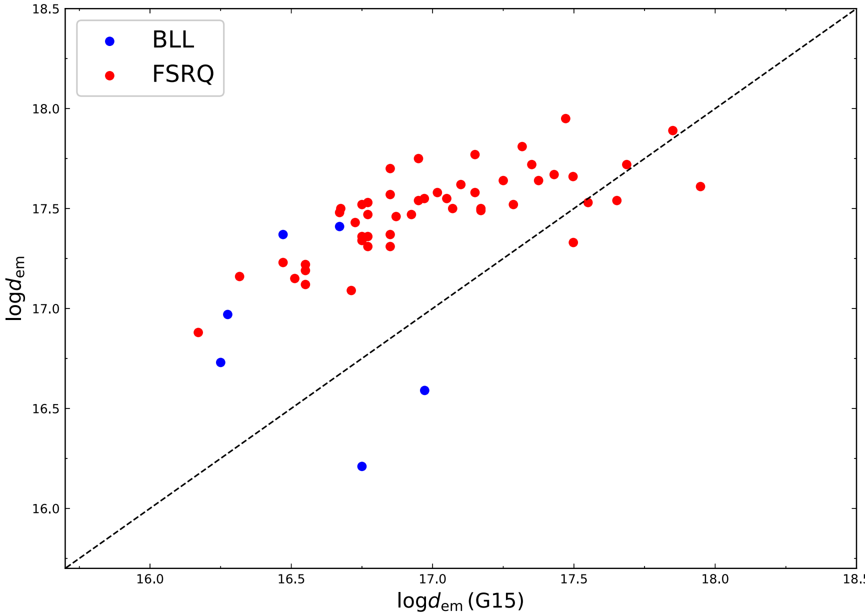

Figure 5. The comparison of $\log d_{em}$ from this work and from Ghisellini & Tavecchio (2015).

which is suggested as $0.1 < \tan\phi < 0.25$ (Dermer et al. 2009; Ghisellini & Tavecchio 2009). Meanwhile, 116 of 147 FSRQs (which is 78.9%) and 20 of 35 BL Lacs (which is 57.1%) have $\tan\phi \leqslant 0.1$. In this case, our result suggests that maybe the viewing angle is smaller than the actual semi-opening angle and the line of sight should lie within the jet cone.

As we can see from the bottom panel of Figure 3, the distributions show that the emission region is located at a distance of 1.68×10^{14} cm to 6.61×10^{19} cm, corresponding to 5.4×10^{-5} pc to 21.3 pc, for all blazars. This large variance of six orders of magnitude directly arises from the variance of the viewing angle, from 0.04 for 4FGL J2035.4+1056 to 84.12 for 4FGL J0113.7+0225. The mean values of $\log d_{em}^{B} = 17.37$ (0.076 pc) for BL Lacs and $\log d_{em}^{F} = 17.49$ (0.1 pc) for FSRQs are very close to each other, and the result of the K-S test confirmed that they are from the same distribution. Figure 5 shows a comparison of $\log d_{em}$ from the present work and from Ghisellini & Tavecchio (2015), in which they estimated the $\log d_{em}$ for 221 sources and gave an average value of $\sim 1 \times 10^{17}$ cm (0.03 pc); the comparison also shows that the $\log d_{em}$ from the present work is larger than those from their work. The comparison result could arise from an underestimated semi-opening angle and thus an overestimated distance from the SMBH. In addition, the different methods we have employed to estimate the $\log d_{em}$ could also generate the discrepancy.

Nevertheless, we check the emission region's relative location with the BLR and DT. The distances from the BLR and from the DT to the SMBH are assumed to scale with the square root of the accretion disk luminosity,

$$d_{BLR} = 10^{17} L_{disk,45}^{1/2} \text{ cm} \tag{11}$$

and

$$d_{DT} = 2.5 \times 10^{18} L_{disk,45}^{1/2} \text{ cm}, \tag{12}$$

where the $L_{disk,45}$ is the accretion disk luminosity L_{disk} in units of 10^{45} erg $\cdot$ s^{-1} (Ghisellini & Tavecchio 2008). The accretion disk luminosity can be estimated by the BLR luminosity $L_{disk} \simeq 10 L_{BLR}$ (Calderone et al. 2013). We manage to collect the L_{BLR} from Xiao et al. (2022b) for 143 of the 182 blazars and list them in Table 2, finding that there are 66 sources (46.2%) with emission regions located within the BLR, 63 sources (44.0%) with emission regions located between the BLR and the DT, and 14 sources (9.8%) with emission regions located beyond the DT. Locating the emission region much farther out of the DT is not appropriate, because there are no important sources of external photons. The reason for the 14 sources with overestimated d_{em} is that small semi-opening angles, less than 0.1, are employed.

To sum up, our results suggest about half of the blazars have emitting regions $d_{em} < d_{BLR}$ and another half have emitting regions $d_{BLR} < d_{em} < d_{DT}$. This is clearly inconsistent with the result suggested in Ghisellini et al. (2014), in which they suggested that 85% of sources have an emission region located within the BLR and 15% of sources have an emission region located between the BLR and the DT. This discrepancy could be caused mainly by two reasons: namely, the sample size and the methods of estimating the d_{em}, while the influence of the method cannot be the main reason, because the deviation caused by one particular method should evenly affect d_{em} for all sources in the sample and should not significantly change the portion of d_{em} within the BLR or within the DT. The best way to eliminate this discrepancy is to compile a larger/complete sample of blazars to estimate the distance from the SMBH to the emission region and determine the emission region's relative location to the BLR or the DT.

5. Conclusions

In order to study the properties of the blazar emission region and put constraints on the corresponding parameters, we compiled a sample of 2708 Fermi blazars with available broadband SED features. A fraction of the sources in our sample also have available redshift, Doppler factor, viewing angle, and BLR luminosity. With the abovementioned information, we calculated the magnetic field ($\log B$) and electron energy ($\log \gamma_p$) for certain types of blazars (FSRQs and

BL Lacs) and provided ranges of $\log B$ and $\log \gamma_{\rm p}$ for BCUs, as well as the electron energy density ($\log U_{\rm e}$), the energy ratio ($\log(U_{\rm e}/U_{\rm B})$), and the critical magnetic strength ($B_{\rm c}$) to study the jet launching and seed variability. A distance ($d_{\rm em}$) from the SMBH to the emission region is obtained for a subsample of 182 sources and used to discuss the emission region location compare to the BLR.

Our main conclusions are as follows. (1) The FSRQs show lower electron energy than the BL Lacs; we suggest dividing FSRQs from BL Lacs with $\log \gamma_{\rm p} = 3.20 \pm 0.01$. Besides, the FSRQs show trends of having a stronger magnetic field and smaller electron-to-magnetic energy ratio than the BL Lacs. (2) Our results suggest that the BL Lacs with a mean value of $\log(U_{\rm e}^{\rm B}/U_{\rm B}^{\rm B}) = 0.98$ may fulfill the equipartition between the magnetic field energy density and the electron energy density, while the FSRQs with a mean value of $\log(U_{\rm e}^{\rm F}/U_{\rm B}^{\rm F}) = -6.45$ are away from the condition $\log(U_{\rm e}/U_{\rm B}) \sim 0$. (3) Comparing the B and $B_{\rm c}$, we find 682 blazars with the B smaller than the $B_{\rm c}$ and suggest these sources are all candidates for showing Kelvin–Helmholtz instability. But we note that our result is an old line and the rest of the blazars could also have a chance of showing this instability. (4) Our result of the location of the blazar emission region is particularly novel. The result suggests that both FSRQs and BL Lacs have emission regions at a distance of ∼0.1 pc. And we find that about half of the blazars have emission regions within the BLR, while another half of the sources have emission regions located between the BLR and the DT.

Acknowledgments

J.H.F. is grateful for support from the NSFC (NSFC U2031201, NSFC 11733001, and U2031112), Scientific and Technological Cooperation Projects (2020–2023) between the People's Republic of China and the Republic of Bulgaria, the Guangdong Major Project of Basic and Applied Basic Research (grant No. 2019B030302001), the science research grants from the China Manned Space Project with No. CMS-CSST-2021-A06, and the support for Astrophysics Key Subjects of Guangdong Province and Guangzhou City. This research was partially supported by the Bulgarian National Science Fund of the Ministry of Education and Science under grants KP-06-H38/4 (2019), KP-06-KITAJ/2 (2020), and KP-06-H68/4 (2022). H.B.X. acknowledges the support from the National Natural Science Foundation of China (NSFC 12203034) and from the Shanghai Science and Technology Fund (22YF1431500).

ORCID iDs

Junhui Fan https://orcid.org/0000-0002-5929-0968
Hubing Xiao https://orcid.org/0000-0001-8244-1229
Lixia Zhang https://orcid.org/0000-0003-3184-6896
Rumen S. Bachev https://orcid.org/0000-0002-0766-864X
Jianghe Yang https://orcid.org/0000-0002-4469-9672

References

Abdo, A. A., Ackermann, M., Agudo, I., et al. 2010, ApJ, 716, 30
Abdollahi, S., Acero, F., Ackermann, M., et al. 2020, ApJS, 247, 33
Acharyya, A., Chadwick, P. M., & Brown, A. M. 2021, MNRAS, 500, 5297
Aharonian, F., Akhperjanian, A. G., Bazer-Bachi, A. R., et al. 2007, ApJL, 664, L71
Albert, J., Aliu, E., Anderhub, H., et al. 2007, ApJ, 669, 862
Amaya-Almazán, R. A., Chavushyan, V., & Patiño-Álvarez, V. M. 2022, ApJ, 929, 14
Barniol Duran, R., Tchekhovskoy, A., & Giannios, D. 2017, MNRAS, 469, 4957
Beck, R., & Krause, M. 2005, AN, 326, 414
Blandford, R. D., & Koenigl, A. 1979, ApL, 20, 15
Blandford, R. D., McKee, C. F., & Rees, M. J. 1977, Natur, 267, 211
Blandford, R. D., & Payne, D. G. 1982, MNRAS, 199, 883
Burbidge, G. R. 1959, ApJ, 129, 849
Cai, J. T., Kurtanidze, S. O., Liu, Y., et al. 2022, ApJS, 260, 47
Calderone, G., Ghisellini, G., Colpi, M., & Dotti, M. 2013, MNRAS, 431, 210
Camenzind, M., & Krockenberger, M. 1992, A&A, 255, 59
Cao, X., & Spruit, H. C. 2013, ApJ, 765, 149
Cerruti, M., Zech, A., Boisson, C., & Inoue, S. 2015, MNRAS, 448, 910
Chen, L. 2014, ApJ, 788, 179
Chen, L. 2017, ApJ, 842, 129
Chen, L. 2018, ApJS, 235, 39
Dermer, C. D. 1999, APh, 11, 1
Dermer, C. D., Cerruti, M., Lott, B., Boisson, C., & Zech, A. 2014, ApJ, 782, 82
Dermer, C. D., Finke, J. D., Krug, H., & Böttcher, M. 2009, ApJ, 692, 32
Dermer, C. D., Yan, D., Zhang, L., Finke, J. D., & Lott, B. 2015, ApJ, 809, 174
Diltz, C., Böttcher, M., & Fossati, G. 2015, ApJ, 802, 133
Dimitrakoudis, S., Mastichiadis, A., Protheroe, R. J., & Reimer, A. 2012, A&A, 546, A120
Fan, J. H. 1999, MNRAS, 308, 1032
Fan, J.-H. 2002, PASJ, 54, L55
Fan, J.-H. 2005, ChJAS, 5, 213
Fan, J.-H., Bastieri, D., Yang, J.-H., et al. 2014, RAA, 14, 1135
Fan, J. H., Kurtanidze, S. O., Liu, Y., et al. 2021, ApJS, 253, 10
Fan, J. H., Tao, J., Liu, Y., et al. 2018, AJ, 155, 90
Fan, J. H., Xie, G. Z., Pecontal, E., Pecontal, A., & Copin, Y. 1998, ApJ, 507, 173
Fan, J. H., Yang, J. H., Liu, Y., et al. 2016, ApJS, 226, 20
Fan, J.-H., Yang, J.-H., Liu, Y., & Zhang, J.-Y. 2013, RAA, 13, 259
Foschini, L., Ghisellini, G., Tavecchio, F., Bonnoli, G., & Stamerra, A. 2011, A&A, 530, A77
Ghisellini, G., & Celotti, A. 2001, MNRAS, 327, 739
Ghisellini, G., Celotti, A., Fossati, G., Maraschi, L., & Comastri, A. 1998, MNRAS, 301, 451
Ghisellini, G., Padovani, P., Celotti, A., & Maraschi, L. 1993, ApJ, 407, 65
Ghisellini, G., & Tavecchio, F. 2008, MNRAS, 387, 1669
Ghisellini, G., & Tavecchio, F. 2009, MNRAS, 397, 985
Ghisellini, G., & Tavecchio, F. 2015, MNRAS, 448, 1060
Ghisellini, G., Tavecchio, F., Maraschi, L., Celotti, A., & Sbarrato, T. 2014, Natur, 515, 376
Giannios, D., & Spruit, H. C. 2006, A&A, 450, 887
Gopal-Krishna, & Wiita, P. J. 1992, A&A, 259, 109
Gupta, A. C., Agarwal, A., Bhagwan, J., et al. 2016, MNRAS, 458, 1127
H. E. S. S. Collaboration, Abramowski, A., Aharonian, F., et al. 2015, A&A, 573, A31
Hovatta, T., O'Sullivan, S., Martí-Vidal, I., Savolainen, T., & Tchekhovskoy, A. 2019, A&A, 623, A111
IceCube Collaboration, Aartsen, M. G., Ackermann, M., et al. 2018, Sci, 361, eaat1378
Kellermann, K. I., Lister, M. L., Homan, D. C., et al. 2004, ApJ, 609, 539
Kellermann, K. I., Sramek, R., Schmidt, M., Shaffer, D. B., & Green, R. 1989, AJ, 98, 1195
Kubo, H., Takahashi, T., Madejski, G., et al. 1998, ApJ, 504, 693
Liodakis, I., Blinov, D., Potter, S. B., & Rieger, F. M. 2022, MNRAS, 509, L21
Liodakis, I., Hovatta, T., Huppenkothen, D., et al. 2018, ApJ, 866, 137
Lister, M. L., Aller, M. F., Aller, H. D., et al. 2015, ApJL, 810, L9
Lister, M. L., Cohen, M. H., Homan, D. C., et al. 2009, AJ, 138, 1874
Lister, M. L., Homan, D. C., Hovatta, T., et al. 2019, ApJ, 874, 43
Lister, M. L., Homan, D. C., Kellermann, K. I., et al. 2021, ApJ, 923, 30
Lynden-Bell, D. 1969, Natur, 223, 690
Massaro, E., Perri, M., Giommi, P., & Nesci, R. 2004, A&A, 413, 489
Massaro, E., Tramacere, A., Perri, M., Giommi, P., & Tosti, G. 2006, A&A, 448, 861
Mücke, A., & Protheroe, R. J. 2001, APh, 15, 121
MAGIC Collaboration, Albert, J., Aliu, E., et al. 2008, Sci, 320, 1752
Nalewajko, K. 2013, MNRAS, 430, 1324
Otero-Santos, J., Acosta-Pulido, J. A., Becerra González, J., et al. 2022, MNRAS, 511, 5611
Pacholczyk, A. G. 1970, Radio Astrophysics. Nonthermal Processes in Galactic and Extragalactic Sources (San Francisco, CA: Freeman)

Paliya, V. S., Domínguez, A., Ajello, M., Olmo-García, A., & Hartmann, D. 2021, ApJS, 253, 46
Pei, Z., Fan, J., Yang, J., Huang, D., & Li, Z. 2022, ApJ, 925, 97
Pei, Z.-Y., Fan, J.-H., Liu, Y., et al. 2016, Ap&SS, 361, 237
Porth, O., & Komissarov, S. S. 2015, MNRAS, 452, 1089
Poutanen, J., & Stern, B. 2010, ApJL, 717, L118
Readhead, A. C. S. 1994, ApJ, 426, 51
Rees, M. J. 1984, ARA&A, 22, 471
Romero, G. E. 1995, Ap&SS, 234, 49
Scarpa, R., & Falomo, R. 1997, A&A, 325, 109
Shukla, A., & Mannheim, K. 2020, NatCo, 11, 4176
Sikora, M., Begelman, M. C., & Rees, M. J. 1994, ApJ, 421, 153
Singh, K. K., & Meintjes, P. J. 2020, AN, 341, 713
Sokolov, A., & Marscher, A. P. 2005, ApJ, 629, 52
Sol, H., Pelletier, G., & Asseo, E. 1989, MNRAS, 237, 411
Strittmatter, P. A., Hill, P., Pauliny-Toth, I. I. K., Steppe, H., & Witzel, A. 1980, A&A, 88, L12
Tan, C., Xue, R., Du, L.-M., et al. 2020, ApJS, 248, 27
Tavecchio, F., & Ghisellini, G. 2008, MNRAS, 386, 945
Tavecchio, F., Maraschi, L., & Ghisellini, G. 1998, ApJ, 509, 608
Tramacere, A., Massaro, E., & Taylor, A. M. 2011, ApJ, 739, 66
Urry, C. M. 1996, in ASP Conf. Ser. 110, Blazar Continuum Variability, ed. H. R. Miller, J. R. Webb, & J. C. Noble (San Francisco, CA: ASP), 391
Urry, C. M., & Padovani, P. 1995, PASP, 107, 803
Villata, M., Raiteri, C. M., Balonek, T. J., et al. 2006, A&A, 453, 817
Wagner, S. J., & Witzel, A. 1995, ARA&A, 33, 163
Wang, G., Fan, J., Xiao, H., & Cai, J. 2022a, PASP, 134, 104101
Wang, Z.-R., Liu, R.-Y., Petropoulou, M., et al. 2022b, PhRvD, 105, 023005
Wardle, J. 2018, Galax, 6, 5
Webb, J. R., Arroyave, V., Laurence, D., et al. 2021, Galax, 9, 114
Wills, B. J., Wills, D., Breger, M., Antonucci, R. R. J., & Barvainis, R. 1992, ApJ, 398, 454
Xiao, H., Fan, J., Ouyang, Z., et al. 2022a, ApJ, 936, 146
Xiao, H., Fan, J., Rando, R., Zhu, J., & Hu, L. 2020, AN, 341, 462
Xiao, H., Fan, J., Yang, J., et al. 2019, SCPMA, 62, 129811
Xiao, H., Ouyang, Z., Zhang, L., et al. 2022b, ApJ, 925, 40
Xiao, H., Zhu, J., Fu, L., Zhang, S., & Fan, J. 2022c, PASJ, 74, 239
Xiao, H. B., Zhu, J. T., Fan, J. H., et al. 2022d, MNRAS, 517, 4202
Xiong, D. R., & Zhang, X. 2014, MNRAS, 441, 3375
Xue, R., Liu, R.-Y., Wang, X.-Y., Yan, H., & Böttcher, M. 2019, ApJ, 871, 81
Xue, R., Liu, R.-Y., Wang, Z.-R., Ding, N., & Wang, X.-Y. 2021, ApJ, 906, 51
Yang, J., Fan, J., Liu, Y., et al. 2023, SCPMA, 66, 249511
Yang, J. H., Fan, J. H., Liu, Y., et al. 2022, ApJS, 262, 18
Zhang, L., Liu, Y., & Fan, J. 2022, ApJ, 935, 4
Zhang, Y.-W., & Fan, J.-H. 2008, ChJAA, 8, 385
Zhu, J. T., Lin, C., Xiao, H. B., et al. 2023, ApJ, 950, 123